Geophysical Journal International

Geophys. J. Int. (2019) **217,** 206–218
Advance Access publication 2019 January 15
GJI Seismology

doi: 10.1093/gji/ggz020

3-D time-domain Gauss–Newton full waveform inversion for near-surface site characterization

Khiem T. Tran,[1] MajidMirzanejad,[1] Michael McVay[1] and David Horhota[2]

[1]*Department of Civil and Coastal Engineering,* 365 *Weil Hall, P.O. Box* 116580*, Gainesville, FL* 32611*, USA. E-mail: ttk@ufl.edu*
[2]*State Geotechnical Engineer, PhD, Florida Department of Transportation,* 5007 N.E. 39th Avenue Gainesville, FL 32609, USA

Accepted 2019 January 11. Received 2019 January 4; in original form 2018 July 09

SUMMARY

We present a new 3-D time-domain Gauss–Newton full waveform inversion (3-D FWI) method for near-surface site characterization. The method is based on a solution of 3-D elastic wave equations for forward modelling of wave propagation, and Gauss–Newton inversion approach for model updating to extract material property. Both the forward modelling and model updating are conducted in the time domain, which allows exploiting complete waveform information of multiple frequencies simultaneously for detailed subsurface material properties. Based on virtual sources and reciprocal wavefields, an efficient approach is developed to calculate derivative seismograms (Jacobian matrix) for all cells simultaneously. The capability of the presented FWI method is tested on both synthetic and field experimental data sets. Sensors and sources located in uniform 2-D grids on the ground surface are used to acquire seismic wavefields, which are then inverted for extraction of 3-D subsurface wave velocity structures. The results show that the waveform analysis was able to characterize low- and high-velocity synthetic layers, and variable soil/rock layers of the test site. The *S*-wave velocity (*Vs*) profiles from field experiment generally agree with invasive standard penetration test (SPT) *N*-values, including identification of a low-velocity zone. *Vs* profiles obtained from a cross-adjoint 3-D FWI are also included for comparison, and results from the presented Gauss–Newton inversion are more consistent with the SPT *N*-values in both trend and magnitudes.

Key words: 3-D full waveform inversion; geotechnical site characterization; 3-D elastic wave equation; Gauss–Newton inversion; wavefield derivatives; virtual source and reciprocity.

1 INTRODUCTION

Full waveform tomography is becoming an efficient geophysical tool for subsurface site characterization at various length scales from metres to kilometres. As documented by Vireux & Operto (2009), the full waveform approach potentially produces higher resolution models of subsurface structures than approaches that consider portions of measured wavefields such as the dispersive characteristic of Rayleigh waves or first-arrival times of body waves. The waveform tomography can be used to identify and quantify embedded anomalies (weak soil or void) and characterize variable soil/rock layers, as phase and magnitude of seismic waves are modulated by the anomalies, layer interfaces and material property variations. Both *S*- and *P*-wave velocities (*Vs* and *Vp*) of the subsurface structures can be extracted independently from measured wavefields to increase credibility of characterized profiles.

A number of 3-D FWI algorithms have been developed and applied to both synthetic and field seismic data at kilometre-scales (Ben-Hadj-Ali *et al.* 2008; Epanomeritakis *et al.* 2008; Fichtner *et al.* 2009; Plessix 2009; Sirgue *et al.* 2010; Tape *et al.* 2010; Vigh *et al.* 2011; Warner *et al.* 2013; Ha *et al.* 2015; Métivier *et al.* 2016). The 3-D FWI algorithms often use acoustic wave equations due to challenging computation, and neglect any elastic effects. The acoustic approximation generally performs well for marine hydrophone data but is limited for land seismic data due to the importance of shear waves (Butzer *et al.* 2013) for geotechnical site investigation. Currently, studies with elastic 3-D FWI analysis are still rare.

At smaller length scales (0–100 m), only a few 3-D FWI studies have been reported for synthetic data (Butzer *et al.* 2013; Fathi *et al.* 2015) and field data (Fathi *et al.* 2016; Nguyen & Tran 2018). The main challenges at small scales include dominant Rayleigh wave components, inconsistent wave excitation (e.g. using sledge-hammers), strong attenuation due to soil viscosity, and strong variability of soil/rock lithology. These challenges have prevented FWI techniques from being used routinely for near-surface site characterization (Tran & Luke 2017). FWI techniques based on the steepest-descent or conjugate gradient methods often create inversion artifacts within a few metres of the ground surface, as well as near source and receiver locations. Dominant Rayleigh waves propagating horizontally near the ground surface produce large derivative seismograms (high sensitivity) with respect to shallow

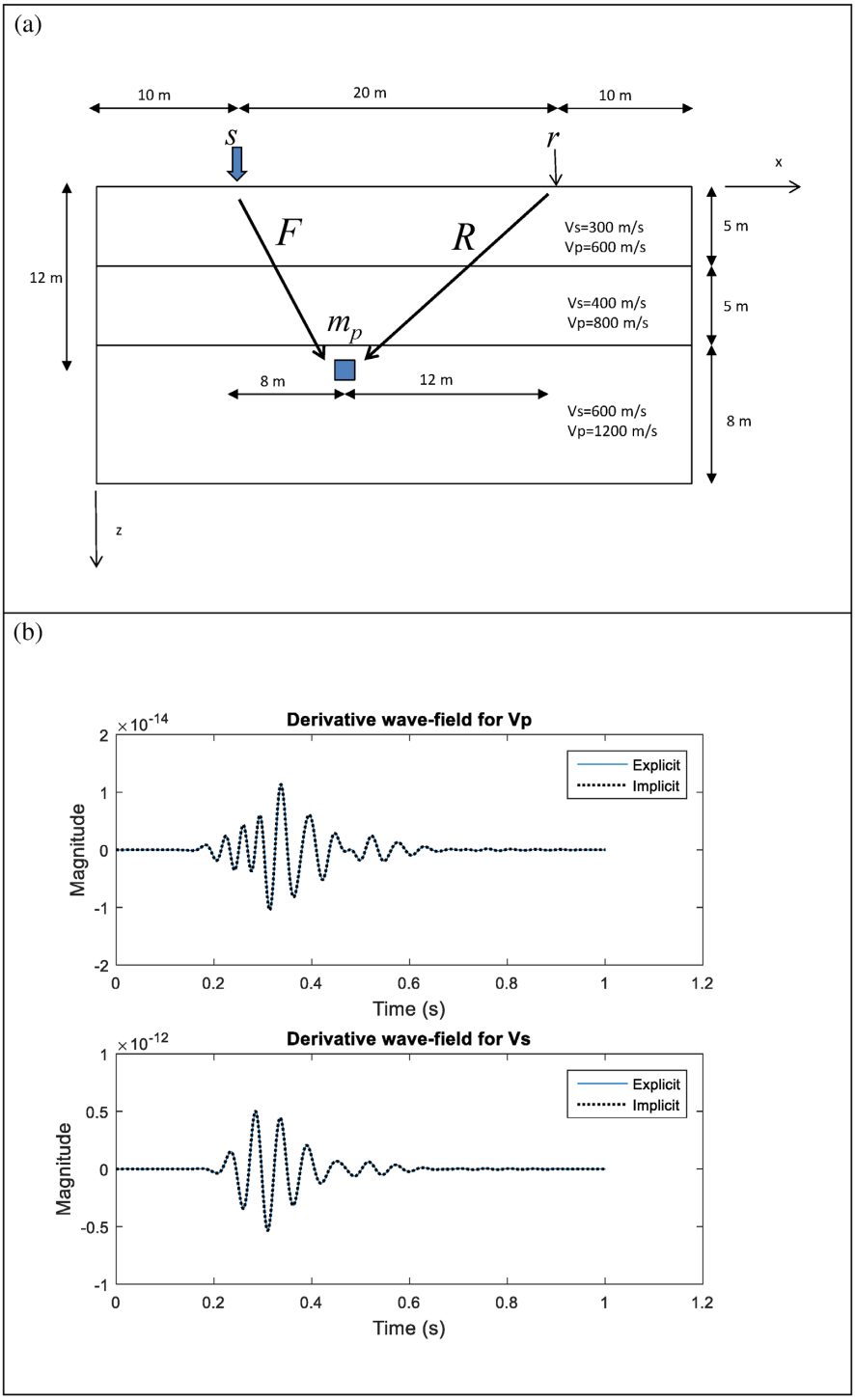

Figure 1. Derivative wavefield comparison: (a) schematic diagram of the model, *s* and *r* denote for vertical source and vertical receiver; and (b) derivative wavefields with respect to *Vp* and *Vs* of a cell at 12 m depth calculated by eq. (8) (Explicit) and eq. (15) (Implicit).

cells. The high sensitivity coupled with large residuals due to inconsistent source, strong attenuation and strong soil/rock variability often result in overshooting of model updates or shallow artifacts. The shallow artefacts produce local solutions and limit the depth of investigation.

The shallow artefacts could be partially suppressed by using gradient tampering for cells near the source/receiver locations (Nguyen & Tran 2018). Specifically, a tampering radius is used for gradually increasing gradient scales from zero at the source/receiver locations to one at the outside of the sphere. However, it is difficult to select

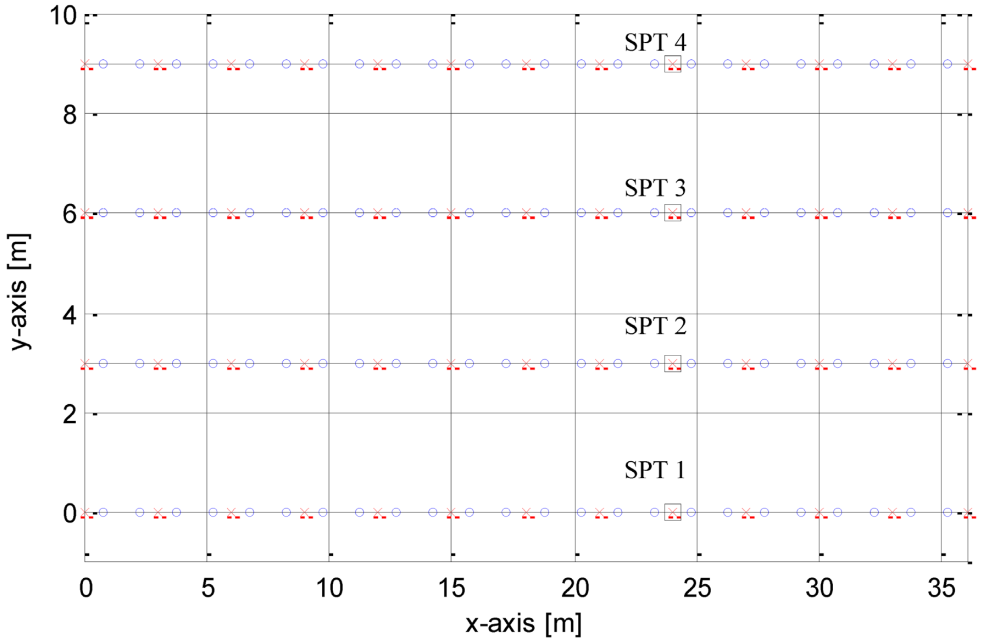

Figure 2. Test configuration used for both synthetic and field experiments: source (cross), receiver (circle). Standard penetration tests, SPT (square) are only for the field experiment.

a proper tampering radius as it depends on quality of measured waveform data, and cells at the source and receiver locations are not updated during inversion.

As an effort to improve field experimental results, this paper presents a new 3-D time-domain Gauss–Newton FWI method for near-surface site investigation (less than 20 m depth). The method is based on 3-D elastic wave equations to simulate particle motion, and Gauss–Newton inversion approach to extract material properties. The seismic wavefields obtained from 2-D grids of sensors and sources on the ground surface are inverted to extract *Vs* and *Vp* structures beneath the test area. The benefits of the time-domain Gauss–Newton inversion include: (1) use of the complete waveform information including multiple frequencies simultaneously for detailed subsurface material properties and (2) the inverse Hessian matrix used in Gauss–Newton inversion acts as a weighting function, which balances the gradient vector to suppress shallow artifacts for better resolution of the deeper stratigraphy (Pratt *et al.* 1998; Sheen *et al.* 2006).

At kilometre-scales with millions of cells, approximations of the inverse Hessian matrix are often used to reduce required computer memory and computing time. Several methods have been developed for the approximations. They include the limited-memory BFGS (L-BFGS, e.g. Nocedal & Wright 2006; Fathi *et al.* 2016), the projected Hessian quasi-Newton (Ma & Hale 2013), the combined Newton and conjugate gradient (Epanomeritakis *et al.* 2008), the pseudo Gauss–Newton (Pan *et al.* 2015) and the truncated Newton (Métivier *et al.* 2013, 2017) methods. Unlike the kilometre-scales, near-surface characterization problems often deal with a much smaller number of cells (tens of thousands). Taking the full advantage of the Gauss–Newton approach, the complete inverse Hessian is used in our presented 3-D FWI algorithm.

The algorithm is first applied to synthetic data generated from a realistic profile consisting of four variable high- and low-velocity soil layers. Subsequently, it is applied to field data collected at a Florida test site and verified with invasive SPT testing. From our best understanding, this is the first reported 3-D time-domain Gauss–Newton FWI for the near-surface site characterization.

2 FULL WAVEFORM INVERSION METHODOLOGY

The developed 3-D FWI method uses forward modelling to generate synthetic wavefields, followed by an inversion to update model parameters. 3-D elastic wave equations are used for the forward modelling, and the Gauss–Newton approach is used to minimize the residual between synthetic (estimated) and measured (observed) wavefields for extraction of material properties (*Vs* and *Vp*).

2.1 Forward modelling of 3-D wave propagation

For the forward modelling, the 3-D elastic wave propagation is described by a set of the first-order linear partial differential equations for isotropic materials. The governing 3-D equations include the force equilibrium (Einstein summation):

$$\rho \dot{v}_i = \sigma_{ij,j} + f_i \tag{1}$$

and the stress–strain or constitutive equations, given as:

$$\rho \dot{\sigma}_{ij} = \lambda v_{k,k} + 2\mu v_{i,j} \qquad \text{if} \quad i = j \tag{2}$$

$$\rho \dot{\sigma}_{ij} = \mu(v_{i,j} + v_{j,i}) \qquad \text{if} \quad i \neq j \tag{3}$$

where σ_{ij} is the ijth component of stress tensor ($i, j = 1, 2, 3$), v_i is the particle velocity, f_i is the external body force, ρ is the mass density and μ, λ are Lamé's coefficients. The over dot (.) denotes the time derivative, and the comma (,) denotes the spatial derivative. For example, $v_{i,j} = \frac{\partial v_i}{\partial x_j}$, is the derivative of the velocity vector with respect to the three spatial coordinates ($x_j = x, y, z$). Also, repetition of a subscript (e.g. k k) denotes summing over the indices (k = 1, 2, 3).

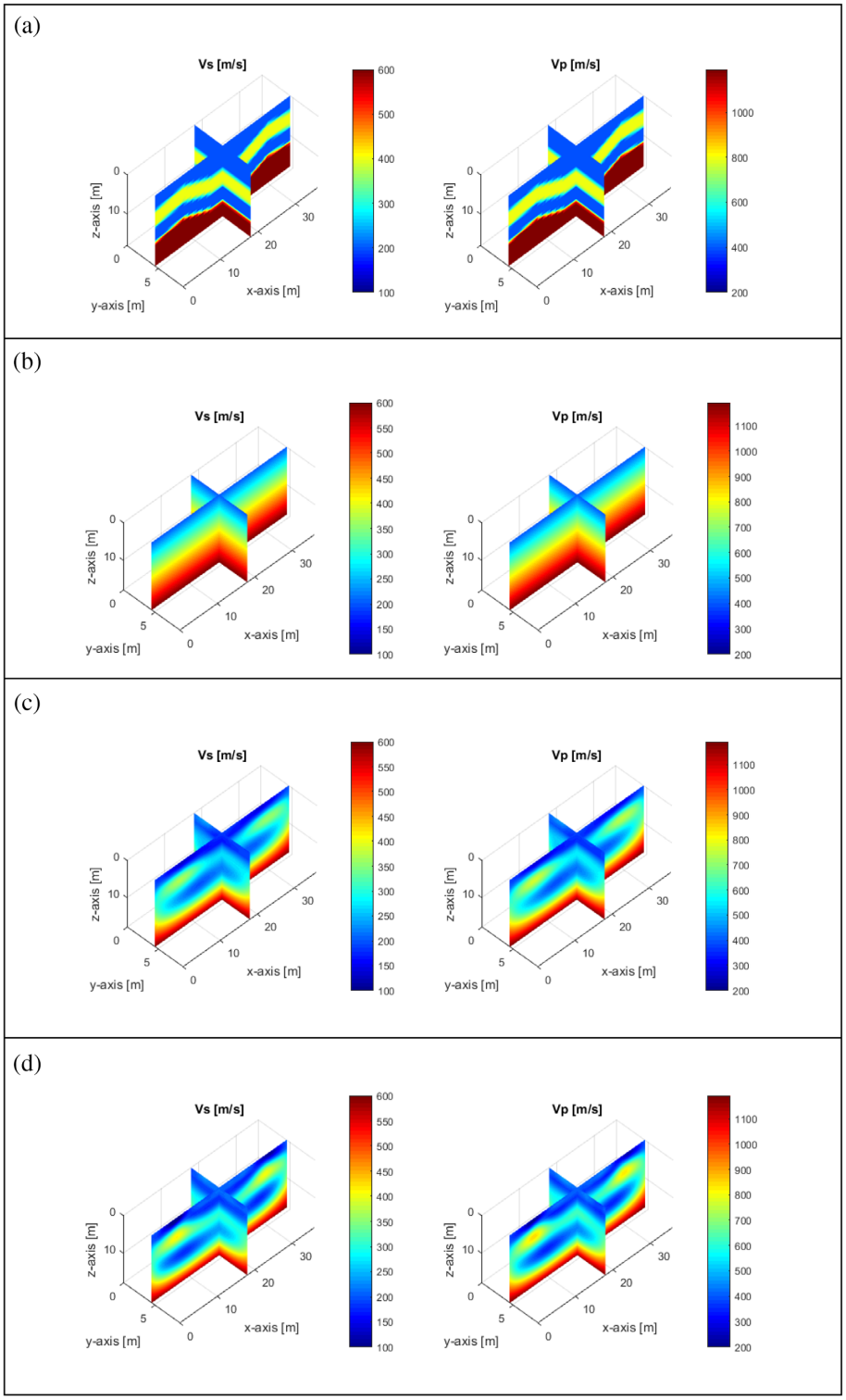

Figure 3. Synthetic model: distribution of *Vs* and *Vp*: (a) true model used to generate synthetic data for inversion analysis; (b) initial model used at the beginning of inversion; and (c) and (d) inverted models with data at 5–20 Hz and 5–30 Hz, respectively.

The classic velocity–stress staggered-grid finite difference method in the time domain (Virieux 1986) was used to solve the equations. The free-surface boundary condition is implemented by using the image technique (Robertsson 1996) at the top boundary (ground surface), while the perfectly matched layer (PML, Komatitsch & Martin 2007) is applied at the vertical and bottom boundaries to absorb outgoing waves. See Nguyen & Tran (2018) for more details.

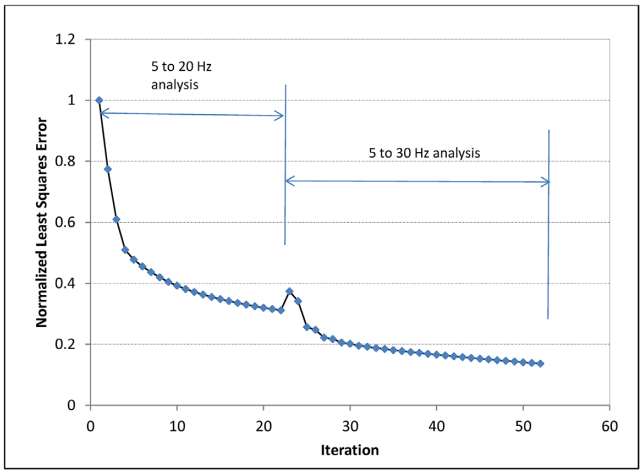

Figure 4. Synthetic model: normalized least squares error versus the iteration number for both inversion runs at 5–20 Hz and 5–30 Hz. The error defines the degree of match between the estimated and observed waveforms during the inversion analysis. The error increases at higher frequencies because the model is not yet appropriate to produce the recorded wave propagation of shorter wavelengths.

2.2 Model updating by Gauss–Newton method

The Gauss–Newton method involves minimizing the residual between the estimated waveform data obtained by forward simulation and the observed seismic data from field testing. The residual is defined as:

$$\Delta \mathbf{d}_{s,r} = \mathbf{F}_{s,r}\ (\mathbf{m}) - \mathbf{d}_{s,r}, \tag{4}$$

where indices s and r denote the sth shot and rth receiver, respectively. The column vector $\mathbf{F}_{s,r}\ (\mathbf{m})$ is estimated waveform data associated with the model $\mathbf{m}$, and obtained from the solution of the wave equations described by eqs (1)–(3). Model $\mathbf{m}$ is a column vector consisting of Vs and Vp of all cells within the modelled test domain. The column vector $\mathbf{d}_{s,r}$ is observed data for the sth shot and rth receiver. Both shots and receivers are located in 2-D uniform grids on the ground surface.

To minimize the residual, a least-squares error E($\mathbf{m}$) is introduced as:

$$\begin{aligned} \mathrm{E}(\mathbf{m}) &= \frac{1}{2}\ \| \Delta \mathbf{d} \|^2 = \frac{1}{2}\ \Delta \mathbf{d}^t \Delta \mathbf{d},\ and\ \Delta \mathbf{d} \\ &= \left\{ \Delta \mathbf{d}_{s,r},\ s = 1..NS, r = 1 \ldots NR \right\}, \end{aligned} \tag{5}$$

where the superscript t denotes the matrix transpose. NS and NR are the numbers of shots and receivers, and $\Delta \mathbf{d}$ is a column vector, which is the combination of residuals $\Delta \mathbf{d}_{s,r}$ for all shots and receivers. The size of $\Delta \mathbf{d}$ is $NT \times NS \times NR$, where NT is the number of time steps. The updated model, $\mathbf{m}^{n+1}$, is obtained from the Gauss–Newton approach for minimization of the error E($\mathbf{m}$) at the (n+1)th iteration from the nth iteration as:

$$\mathbf{m}^{n+1} = \mathbf{m}^n - \alpha^n \left[\mathbf{J}^t \mathbf{J} + \lambda_1 \mathbf{P}^t \mathbf{P} + \lambda_2 \mathbf{I}^t \mathbf{I} \right]^{-1} \mathbf{J}^t \Delta \mathbf{d}, \tag{6}$$

where $\mathbf{J}$ is the Jacobian matrix, or the partial derivative of wavefield with respect to individual model parameters (Vs and Vp of cells). The detailed calculation of matrix $\mathbf{J}$ is presented in the following section. $\mathbf{I}$ is the identity matrix, and $\mathbf{P}$ is a matrix, whose elements are determined using a 3-D Laplacian operator:

$$\begin{aligned} P_p\ (\Delta m) = &\left(\Delta m_p\right)^L + \left(\Delta m_p\right)^R + \left(\Delta m_p\right)^F + \left(\Delta m_p\right)^B \\ &+ \left(\Delta m_p\right)^A + \left(\Delta m_p\right)^U - 6\left(\Delta m_p\right) \Delta, \end{aligned} \tag{7}$$

where the superscripts L, R, F, B, A and U refer to six adjacent cells (left, right, front, back, above and under) of the cell referring to the model parameter m_p, and P_p is the pth row of the matrix $\mathbf{P}$ whose elements are either 1, –6 or 0. Coefficients λ_1 and λ_2 are constants, which are used for regularization to increase the invertability of the approximate Hessian matrix ($\mathbf{H_a} = \mathbf{J^t J}$). The choice of the coefficients from 0 to infinity represents a compromise. Larger values of λ_1 and λ_2 lead to smoother inverted models (not good for characterizing of material contrast), whereas smaller values produce more inversion artefacts. Several trial runs were conducted in the study, with $\lambda_1 = 0.02$ and $\lambda_2 = 0.0005$ giving good results for both the synthetic and field data sets. The step length α^n is generally close to 1.0, and it is fixed at 1.0 for this study.

To save computer time, the term $[\mathbf{J}^t\mathbf{J}+\lambda_1\mathbf{P}^t\mathbf{P}+\lambda_2\mathbf{I}^t\mathbf{I}\,]^{-1}\mathbf{J}^t\Delta\mathbf{d}$ in eq. (6) is calculated using the LU decomposition by a Matlab built-in function, which does not require to compute the inverse of the Hessian matrix explicitly. This term is calculated for Vs and Vp separately using the according Jacobian matrix $\mathbf{J}$. It is noted that $[\mathbf{J}^t\mathbf{J} + \lambda_1\mathbf{P}^t\mathbf{P} + \lambda_2\mathbf{I}^t\mathbf{I}\,]^{-1}$ acts as a weighting function, and thus no scaling is needed for the gradient vectors of Vs and Vp. Both velocities are updated simultaneously in each iteration.

2.3 Partial derivative wavefield

The main challenge for the use of Gauss–Newton method is the computation of the partial derivative of the wavefield (matrix $\mathbf{J}$). One approach is to take the partial derivative of the wavefield with respect to a model parameter (m_p) for the sth shot and rth receiver explicitly through two forward simulations with and without the model perturbation as:

$$\mathbf{J}^p_{s,r} = \frac{\partial \mathbf{F}_{s,r}\ (\mathbf{m})}{\partial m_p} = \frac{\mathbf{F}_{s,r}\ (\mathbf{m} + \Delta m_p) - \mathbf{F}_{s,r}\ (\mathbf{m})}{\Delta m_p}. \tag{8}$$

By perturbing the individual model parameters (unknowns), a total of $NS \times (M+1)$ forward simulations are required to calculate the matrix $\mathbf{J}$, where M is the number of unknowns. This requires significant computer time, that is many thousands of model parameters within 3-D profiles. Another more efficient approach is to expand the implicit approach developed for 2-D time-domain FWI (Sheen *et al.* 2006; Tran & McVay 2012; Tran *et al.* 2013) to evaluate the derivative of the wavefield for the 3-D problem.

For the model parameters representing the P-wave velocity (Vp), eqs (1)–(3) are differentiated with respect a parameter Vp_n,

$$\rho\ \frac{\partial \dot{v}_i}{\partial Vp_n} = \frac{\partial \sigma_{ij,j}}{\partial Vp_n} \tag{9}$$

$$\rho\ \frac{\partial \dot{\sigma}_{ij}}{\partial Vp_n} = \lambda \frac{\partial v_{k,k}}{\partial Vp_n} + 2\mu \frac{\partial v_{i,j}}{\partial Vp_n} + 2\rho Vp \frac{\partial Vp}{\partial Vp_n} v_{k,k} \quad \text{if} \quad i = j \tag{10}$$

$$\rho\ \frac{\partial \dot{\sigma}_{ij}}{\partial Vp_n} = \mu \left(\frac{\partial v_{i,j}}{\partial Vp_n} + \frac{\partial v_{j,i}}{\partial Vp_n} \right) \quad \text{if} \quad i \neq j \tag{11}$$

and the term $2\rho Vp \frac{\partial Vp}{\partial Vp_n} v_{k,k}$ in eq. (10) represents the virtual source for the partial derivative of wavefield ($\frac{\partial \mathrm{v_i}}{\partial \mathrm{Vp_n}}$) propagated from the parameter Vp_n location to the receivers. It is noted that $\frac{\partial \mathrm{Vp}}{\partial \mathrm{Vp_n}}$ is equal to 1.0 at the parameter location and zeros for the rest of medium, or the virtual source is equal to $2\rho \mathrm{Vp} v_{\mathrm{k,k}}$. Similarly, for the model parameters representing the S-wave velocity (Vs), eqs (1)–(3) are

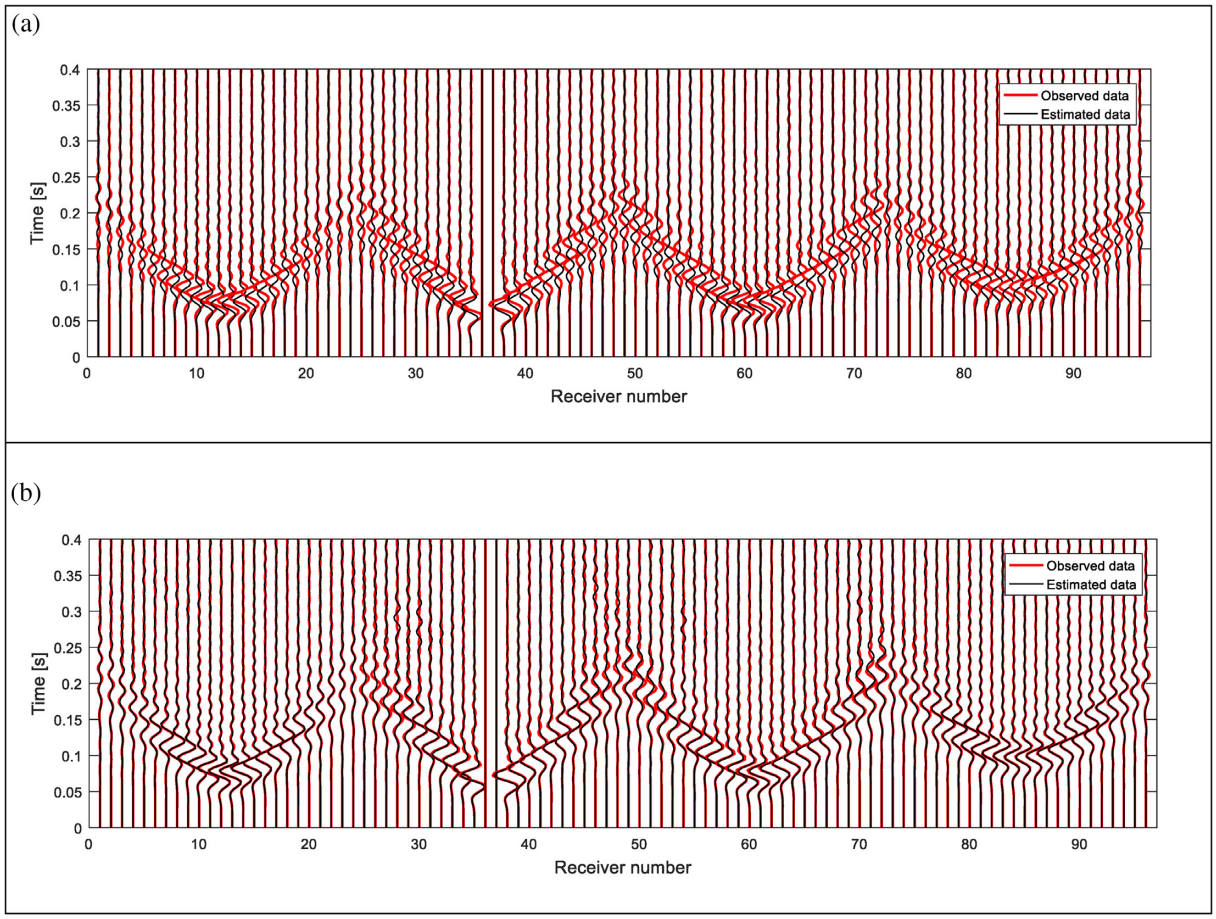

Figure 5. Synthetic model: waveform comparison for a sample shot associated with the initial model (a) and final inverted model (b).

differentiated with respect a parameter Vs_n as:

$$\rho \frac{\partial \dot{v}_i}{\partial Vs_n} = \frac{\partial \dot{\sigma}_{ij,j}}{\partial Vs_n} \tag{12}$$

$$\rho \frac{\partial \dot{\sigma}_{ij}}{\partial Vs_n} = \lambda \frac{\partial v_{k,k}}{\partial Vs_n} + 2\mu \frac{\partial v_{i,j}}{\partial Vs_n} - 4\rho Vs \frac{\partial Vs}{\partial Vs_n}(v_{k,k} - v_{j,i}) \quad \text{if} \quad i = j \tag{13}$$

$$\rho \frac{\partial \dot{\sigma}_{ij}}{\partial Vs_n} = \mu \left(\frac{\partial v_{i,j}}{\partial Vs_n} + \frac{\partial v_{j,i}}{\partial Vs_n} \right) + 2\rho Vs \frac{\partial Vs}{\partial Vs_n}(v_{i,j} + v_{j,i}) \quad \text{if} \quad i \neq j \ . \tag{14}$$

In eqs (13) and (14), a virtual source for the derivative wavefield ($\frac{\partial v_i}{\partial Vs_n}$) at the location of parameter Vs_n is $-4\rho \mathrm{Vs}(v_{\mathrm{k,k}} - v_{\mathrm{j,i}})$ if $i = j$, and $2\rho \mathrm{Vs}(v_{\mathrm{i,j}} + v_{\mathrm{j,i}})$ if $i \neq j$ is introduced.

The same Jacobian component of eq. (8) can be obtained by propagating the virtual sources at the parameter location to the receivers. Also, based on the reciprocity of wave propagation, waveforms are identical if a source and a receiver are switched. Thus, the Jacobian matrix (**J**) can be determined by convolution of the virtual sources and backward wavefields, which are both obtained from forward simulations (eqs 1–3). This approach requires only (*NS*+*NR*) forward simulations for the calculation of matrix **J.** Finally, the partial derivative of the wavefield with respect to a model parameter (m_p) for the sth shot and rth receiver can be implicitly calculated as:

$$\mathrm{J}^p_{s,r} = F_x * R_x + F_y * R_y + F_z * R_z \tag{15}$$

where F_x, F_y and F_z are virtual sources calculated from forward wavefields, which are generated by a source at the sth shot location and recorded at the location of model parameter m_p (eqs 9–14) in directions x, y and z, respectively. R_x, R_y and R_z are backward wavefields generated by a source at the rth receiver location and recorded at the model parameter m_p location in directions x, y and z, respectively. The $*$ denotes the convolution.

For verification, shown in Fig. 1 is a comparison of partial derivative of the wavefields calculated explicitly and implicitly by eqs (8) and (15), respectively. The tested model is 18 × 40 × 40 m (depth × length × width) in z, x and y directions. It consists of three horizontal layers with Vs values of 300, 400, 600 m s^{-1} and Vp values of 600, 800, 1200 m s^{-1}, respectively, as shown in Fig. 1(a) at a vertical plane of y = 20 m (middle of the width). The medium was divided into 1 × 1 × 1 m cells, and a Ricker wavelet source of 15 Hz central frequency was used for wave simulation. The source and receiver are both vertical and located on the free surface (depth 0). The model parameter m_p are Vs and Vp of a cell at depth of 12 m. Shown in Fig. 1(b) are derivative wavefields calculated by eq. (8) (explicit) and eq. (15) (implicit) with respect to Vp and Vs of the cell. It is noted that derivative wavefield calculated by eq. (8) was convolved with the source signature to account for the scale of the source signature used for the backward wavefields in eq. (15). Evident from Fig. 1, the implicit and explicit derivative wavefields are identical, but the implicit approach is much more efficient and used in subsequent work. As the derivative wavefields calculated by eq. (15) are scaled by the source signature

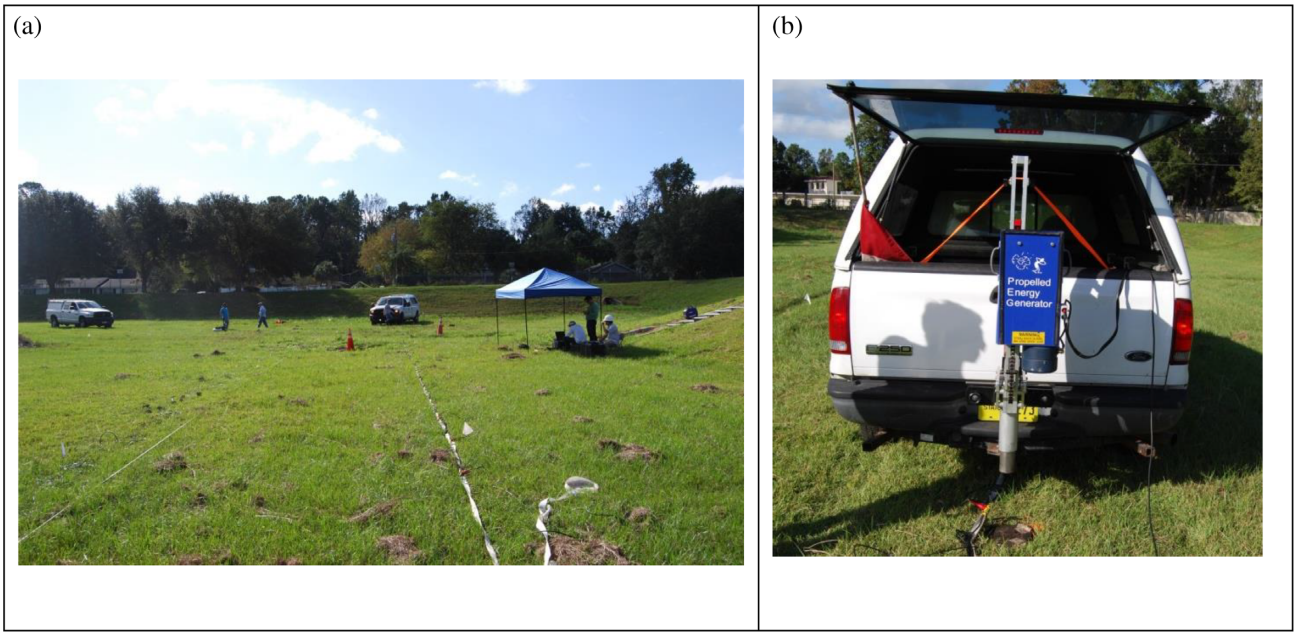

Figure 6. Field experiment: (a) test site and (b) propelled energy generator

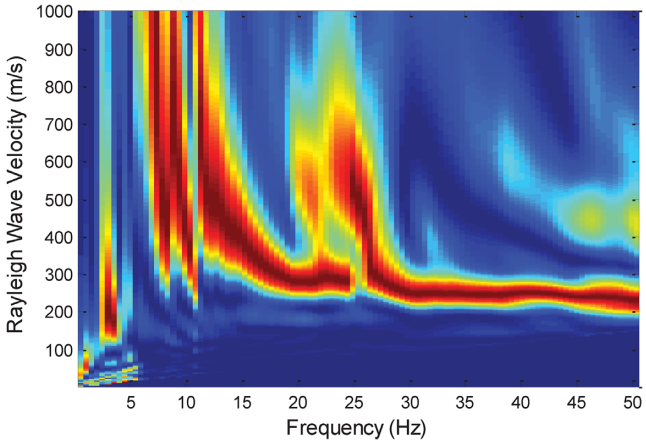

Figure 7. Field experiment: spectral analysis of measured data for one sample shot and one line of 24 geophones.

used for the backward wavefields, the residuals (eq. 4) are convolved with the same source signature before using for model updating in eq. (6).

3 APPLICATION ON SYNTHETIC DATA

The first application of the 3-D inversion was on a synthetic model data set. First, surface-based waveform data was calculated for a test configuration (i.e. 2-D uniform grids of shots and receivers as shown in Fig. 2), and subsequently they were input to the 3-D FWI algorithm as if they were acquired from a field test. Then the *Vs* and *Vp* structures were extracted from the inversion, and compared to the true profile for evaluation of the algorithm.

The 3-D FWI was tested on a realistic model including both high- and low-velocity layers. The model was 18 × 36 × 9 m (depth × length × width), consisting of four soil layers (Fig. 3a) with a low-velocity third layer. The four layers have *Vs* values of 200, 400, 200 and 600 m s^{-1} , and the *Vp* is calculated from *Vs* and a constant Poisson ratio of 1/3 for the entire medium (or *Vp* is twice that of *Vs*). The mass density was 1800 kg m^{-3} for the whole model. Synthetic waveform data were computed using the solution of eqs (1)–(3), with a test configuration of 96 receivers and 52 shots (sources) located in 2-D uniform grids (Fig. 2). The receiver grid was 4 × 24 at 3 m spacing in the shorter direction and 1.5 m spacing in the longer direction, and the source grid was 4 × 13 at 3 m spacing in both directions. Sources and receivers were both vertical and located on the free surface (0-m depth). The Ricker wavelet of 15 Hz central frequency was used for the source signature.

A basic 1-D initial model with *Vs* and *Vp* linearly increased with depth (Fig. 3b) was used for inversion. The *Vs* increased from 200 m s^{-1} on the free surface (0-m depth) to 600 m s^{-1} at the bottom of the model (18-m depth), the *Vp* is twice that of *Vs*. Such an initial model can be established via a spectral analysis of measured data (see the field data application for details). The same data set (created by Ricker wavelet source of 15 Hz central frequency) were filtered through two frequency ranges of 5–20 Hz and 5–30 Hz, and used for the two inversion runs. The two frequency ranges were selected to be consistent with dominant frequency components of the field data (presented later). The first range of 5–20 Hz provided the central frequency of about 10 Hz, and then a bandwidth of 10 Hz (from 20 to 30 Hz) was added for the second range. The first run began with the lower frequency range on the initial model (Fig. 3b), as the lower frequency data have larger wavelengths and produce fewer local minima in the misfit function, thus require a less detailed initial model. The second run was performed with the higher frequency range (5–30 Hz) using the inverted result from the first run as the input model.

Vs and *Vp* values of the individual cells were updated simultaneously by eq. (6) during the inversion analysis. The stopping criterion was set at the point when the least-squares error changed less than 1 per cent from one iteration to the next for three consecutive iterations, or if a preset maximum number of iterations (30) had been reached. The first and second runs stopped after 22 and 30 iterations, respectively. The two runs took approximately 36 hr in total on a computer with 32 cores having 3.46 GHz each and 256 GB of

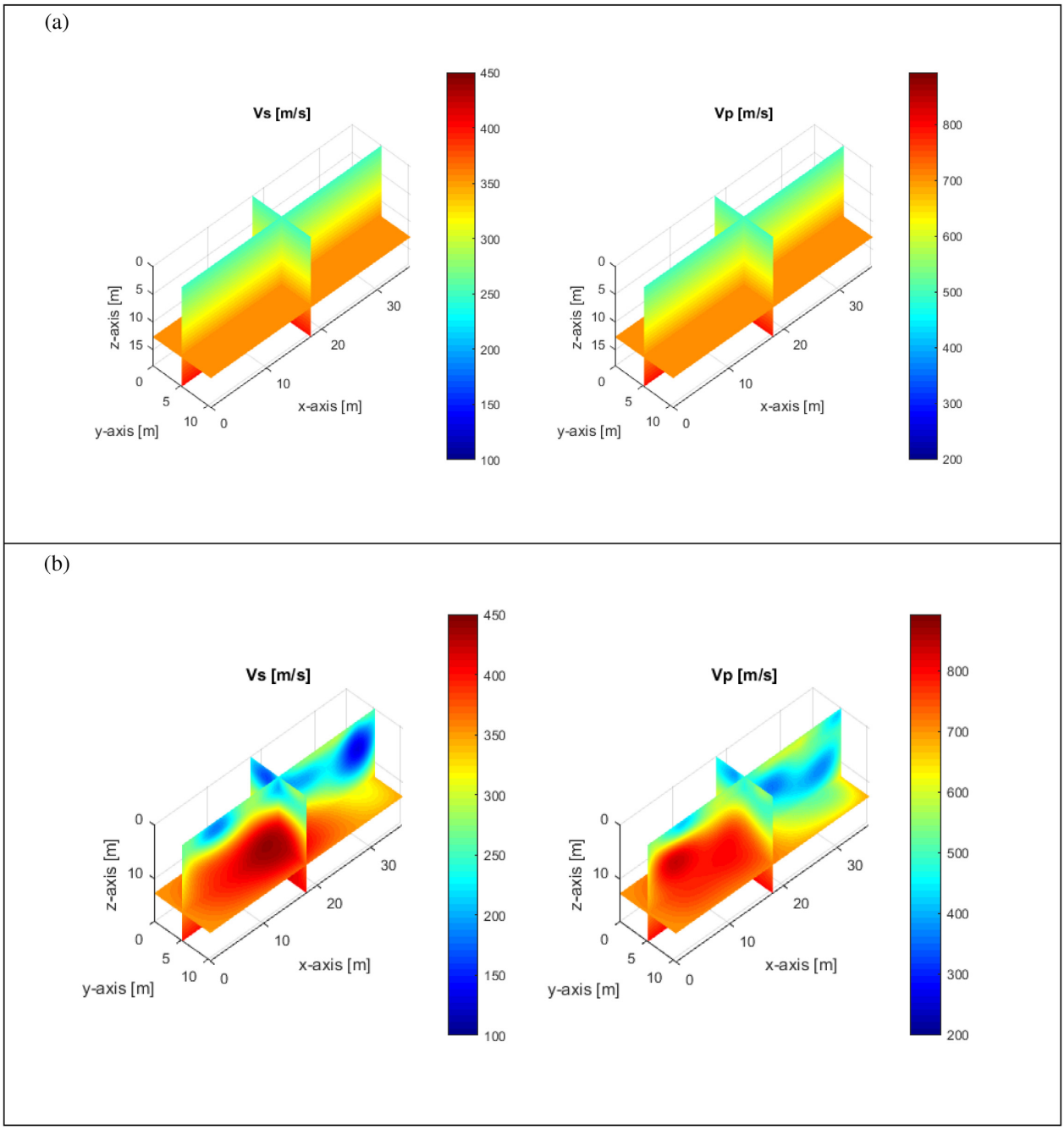

Figure 8. Field experiment: distribution of V_S and V_P (m s^{-1}): (a) initial model used at the beginning of inversion; and (b) final inverted models at 5–30 Hz.

memory; approximately 220 GB of memory was actually used in the analyses.

The least-squares errors for all 52 iterations of the two inversion runs are normalized by the initial error of the first iteration and shown in Fig. 4. The error reduced from 1.0 at the first iteration to less than 0.13 at the final iteration (iteration 52). The error increased when adding data from 20 to 30 Hz, because the model is not yet appropriate to produce the recorded wave propagation of shorter wavelengths. Fig. 5 shows a comparison of observed data at 5–30 Hz, for the estimated data associated with the initial model and the final inverted result at iteration 52. Clearly, the waveform match improved significantly during inversion. The observed and final estimated data (Fig. 5b) agrees well with no cycle skipping (matching of wrong peaks), suggesting that the 1-D initial model is sufficent.

Results of the two inversion runs are shown in Fig. 3. The result at 5–20 Hz (Fig. 3c) is comparable to the true model (Fig. 3a), showing a 4-layer profile in both *Vs* and *Vp* images along with the low-velocity third layer. The result at 5–30 Hz (Fig. 3d) is very similar to the true model (Fig. 3a). The inverted result was improved considerably during the second run by adding the higher frequency data, particularly for the top two layers. The variable layer interfaces were also accurately characterized, and the true *Vs* and *Vp* values of all layers were recovered. It is noted that the inversion results are less accurate at the model edges due to poor signal coverage in these areas.

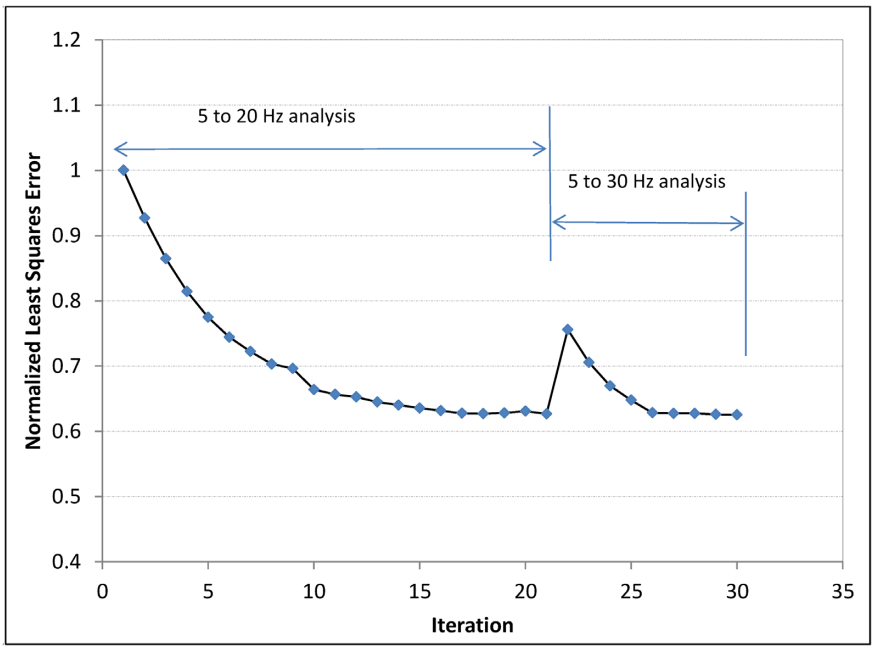

Figure 9. Field experiment: normalized least squares error versus the inversion iteration number for both inversion runs at 5–20 Hz and 5–30 Hz. The error defines the degree of match between the estimated and observed waveforms during the inversion analysis. The error increases at higher frequencies because the model is not yet appropriate to produce the recorded wave propagation of shorter wavelengths.

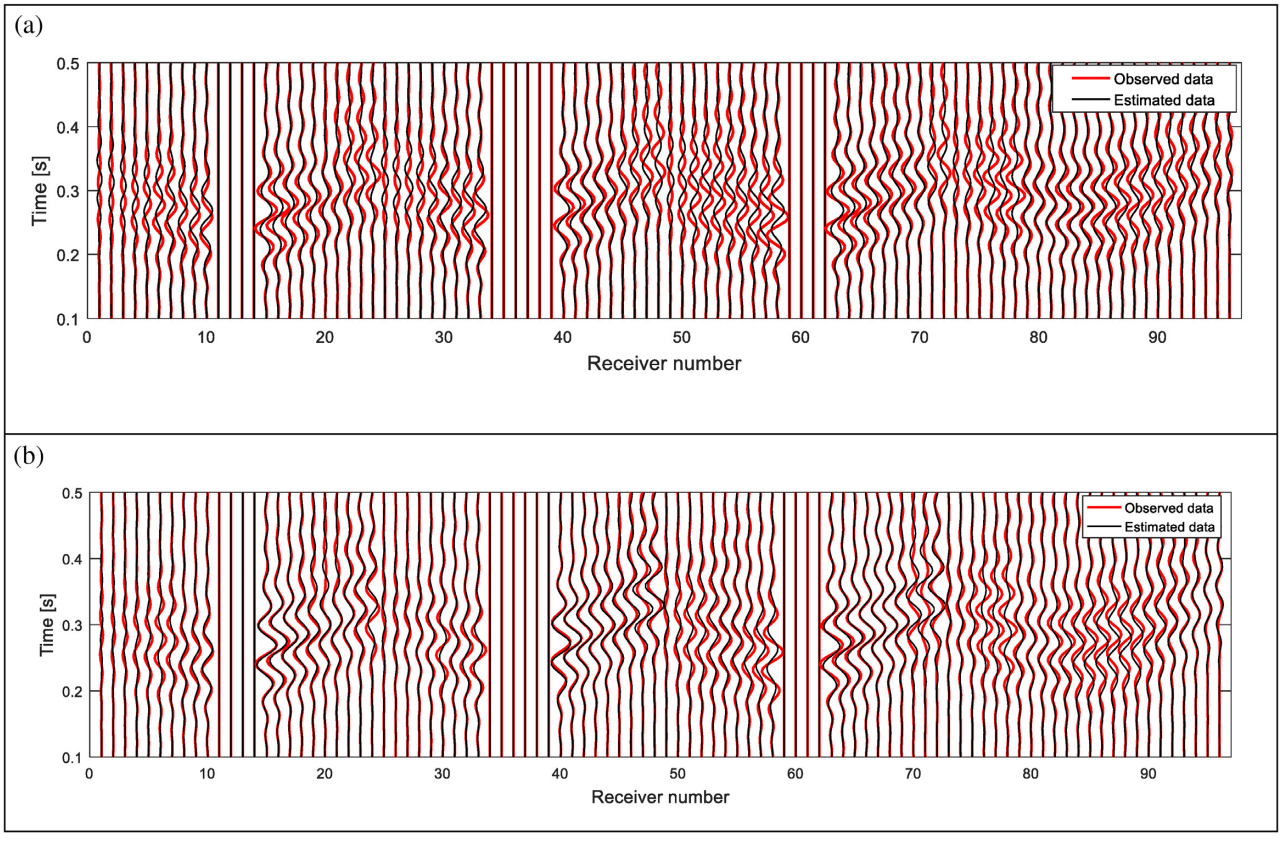

Figure 10. Field experiment: waveform comparison for a sample shot associated with the initial model (a) and final inverted model (b). Poor channels near the source are removed from analysis.

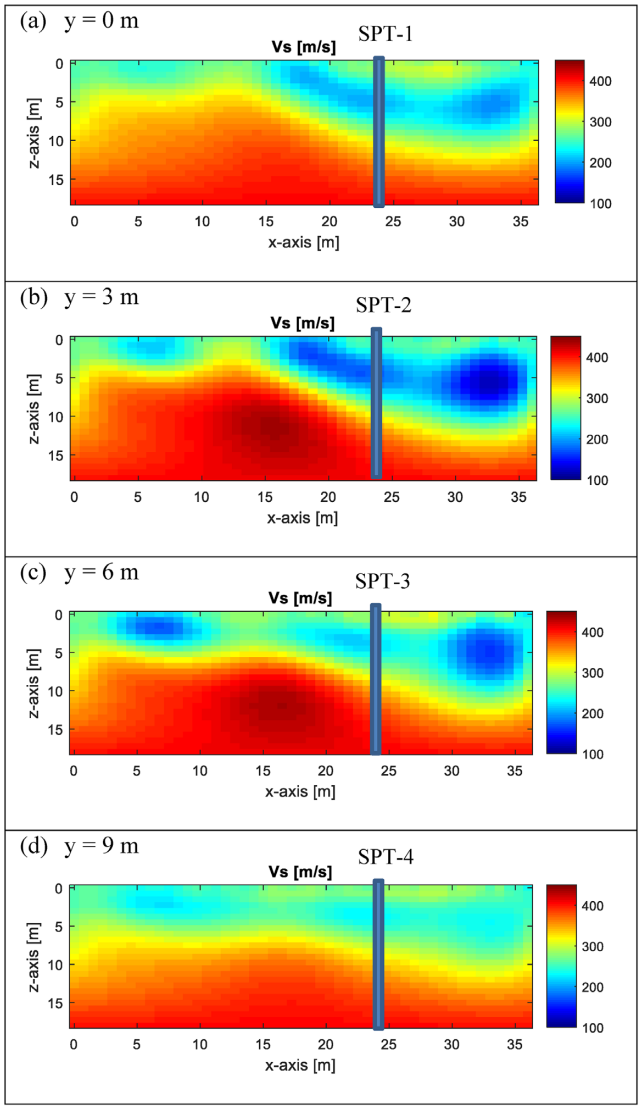

Figure 11. Field experiment: inverted *Vs* and SPT locations along four receiver lines at $y = 0$, 3, 6 and 9 m

4 APPLICATION TO 3-D FIELD DATA

The presented 3-D FWI method was subsequently applied to field experimental data, collected at a dry retention pond in Gainesville, Florida, USA (Fig. 6a). The field experiment was done with the same test configuration of 96 receivers and 52 shots (Fig. 2). The seismic wavefields were generated by a propelled energy generator (PEG, 40 kg model) as shown in Fig. 6(b), and simultaneously recorded by 48 4.5-Hz vertical geophones in two stages. In each stage, the 48 geophones were placed for a half of the receiver grid, and 52 shots were applied for the entire source grid (4 × 13). As the same impact load (same drop weight and height of the PEG) was applied at each shot location, the collected data from the two stages were simply combined to produce 96-channel shot gathers. Four standard penetration tests (SPT) were also conducted at distance of 24 m (x = 24 m) on each geophone line for verification of seismic results. This same data set had been analysed by a cross-adjoint 3-D FWI algorithm (Nguyen & Tran 2018), and the results are also included in this paper for comparison.

As presented by Nguyen & Tran (2018), a 1-D initial model was developed via spectral analysis of the measured data for a sample shot and one line of 24 geophones (Fig. 7). Rayleigh wave velocities (*Vr*) were determined from 250 to 400 m s^{-1} at the frequency range of 12–50 Hz. As *Vs* is similar to *Vr*, the *Vs* near the ground surface associated with high frequency data was known to be approximately 250 m s^{-1} . The half space with *Vs* of 400 m s^{-1} was assumed at the start at a half of maximum wavelength associated with data at 12 Hz or a depth of 16.7 m (velocity/frequency/2 = 400/12/2 = 16.7 m). Similar to the case of synthetic model, the initial model (Fig. 8a) was established having *Vs* increasing with depth from 250 m s^{-1} at the surface to 400 m s^{-1} (*Vs* of the half space) at the bottom of the model. The depth of model was taken as a half of the longer dimension of test area (or 18 m) to maintain good signal coverage in the analysed domain. The *Vp* was estimated from *Vs* and a constant Poisson's ratio of 1/3 for the entire medium, which was taken as the middle value of the range from $\frac{1}{4}$ to $\frac{1}{2}$ for general soils. The mass density was assumed as 1800 kg m^{-3} for the whole medium and kept constant during inversion. Efforts to invert the mass density of medium from the measured wavefield have been shown to be unsuccessful. This can be explained that most of the energy in wavefields measured on the surface are Rayleigh waves that are not very sensitive to the mass density.

Similar to the synthetic data analyses, measured field data were filtered through the two frequency bandwidths of 5–20 Hz and 5–30 Hz, and used in two sequential inversion runs. The first run at 5–20 Hz began with the initial model shown in Fig. 8(a), and the second run began with the inverted result of the first run. During inversion, estimated waveform data are adjusted by an offset-dependent correction factor of the form $y(r) = A \cdot r < \sigma\psi > ^{\alpha})$ to compensate for material damping (inelasticity) that cannot be accounted for with the elastic model. Where r is the source–receiver offset, and the factor A and exponent $<\sigma\psi>\alpha$ were determined with an iterative least-squares inversion, which minimizes the energy of waveform residuals. For forward simulation, a source signature was estimated by deconvolution of the measured data with the Green's function, which was explicitly calculated by forward simulation with an assumed Ricker wavelet source (Tran & Luke 2017). The source signature was updated at the beginning of each iteration to account for the change of Green's function during inversion due to updated model parameters.

The medium of 18 × 36 × 9 m (depth × length × width) was divided into 13 824 cells of 0.75 × 0.75 × 0.75 m. Each 0.75 m cell size was selected as half of the smaller geophone spacing (1.5 m) to conveniently assign sources and receivers to discretized nodes. The same cell size was used for both inversion runs. *Vs* and *Vp* of all cells were updated independently and simultaneously during inversion. The first and second inversion runs stopped at 21 and 9 iterations, respectively. The total computer time was about 26 hr on the same computer used for the synthetic data analyses.

Fig. 9 shows the least-squares errors for all 30 iterations of both inversion runs, which were normalized by the initial error. The error reduced from 1.0 to about 0.62 in the first run, and further in the second run. Again, the error increased when adding data from 20 to 30 Hz, because the model is not yet appropriate to produce shorter wavelength data. Shown in Fig. 10 is a comparison of observed data at 5–30 Hz, and estimated data associated with the initial model and the final inverted result at iteration 30 for a sample shot. The agreement between observed and estimated data improved during inversion. The observed and final estimated waveform data agree well for most channels in Fig. 10(b). No cycle skiping is

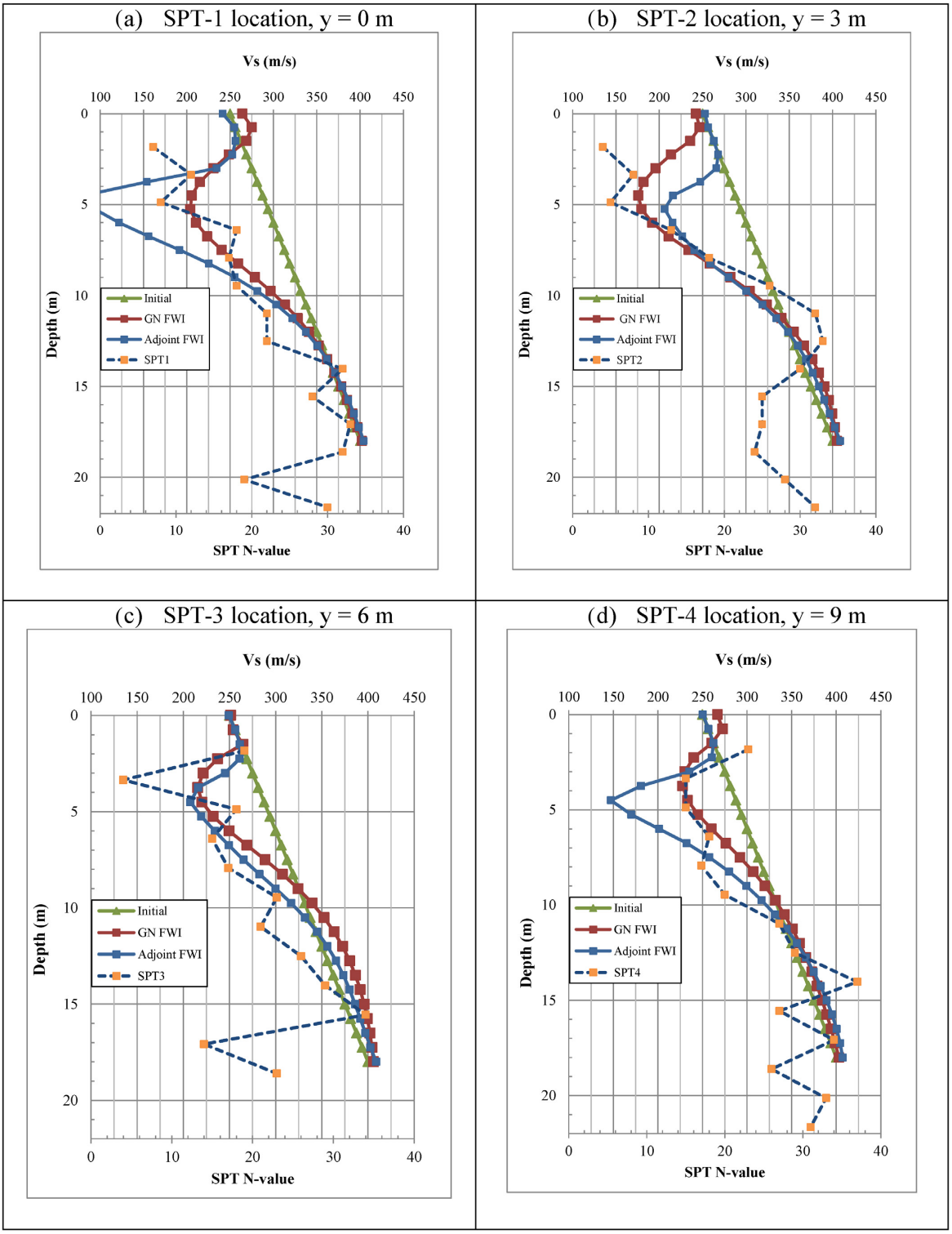

Figure 12. Comparison between *Vs* and SPT N-values at the 4 invasive test locations. GN FWI and Adjoint FWI denote results from Gauss–Newton and cross-adjoint waveform inversion methods, respectively.

observed; suggesting the 1-D initial model established from the spectral analysis was sufficent.

The final inverted results for data at 5–30 Hz are shown in Fig. 8(b). The *Vs* profile (Fig. 8b, top) consists of softer layers (*Vs* ∼150–300 m s^{-1}) with a buried low-velocity zone at about 5-m depth, underlain by a stiffer layer (*Vs* ∼ 400 m s^{-1}). The *Vp* profile (Fig. 10b, bottom) is consistent with the *Vs* profile. Based on soil types from SPT borings, the softer layers and stiffer layer are soils and weathered limestone, respectively. For better viewing, the lateral variation, Fig. 11 shows *Vs* profiles along four receiver lines at y = 0, 3, 6 and 9 m, together with the four SPT locations. Variation of soil layers is consistent along

y direction with shallower weathered limestone in the left of test domain.

Shown in Fig. 12 are the initial *Vs* values, the final inverted *Vs* values at 5–30 Hz, and SPT N-values at four locations. The depths of four SPTs are about 21-m depth. The final inverted *Vs* values are very different from the initial values, suggesting the *Vs* profiles have changed (updated) significantly during inversion analysis, particularly at depths less than 10 m. The final inverted *Vs* and SPT results generally agree at all four locations. Both show soft materials from 0 to 5-m depth, linearly increasing stiffness with depth from 5 to 10-m depth, and stiffer materials below 10-m depth. The low-velocity zone at about 5-m depth identified by the waveform analysis is confirmed by the SPT results, particularly at the SPT-3 and SPT-4 locations. There is discrepancy between the *Vs* (higher values) and SPT N-values at depths less than 2 m of SPT-1 and SPT-2. The discrepancies could be due to local compactions of soil during seismic testing by the truck carrying the seismic source, or more likely due to inversion artifacts near source locations that could not be suppressed by Gauss–Newton inversion. Also, the SPT *N*-values appear more erratic than *Vs* values. This is due to that N-values represent more local properties than do *Vs* values, which are average within cell volumes ($0.75 \times 0.75 \times 0.75$ m each).

Results from this seismic data set analysed by a cross-adjoint 3-D FWI had been reported in details by Nguyen & Tran (2018), in which the same initial model and frequency content were used. The inverted *Vs* from the cross-adjoint inversion at the four SPT locations are also included in Fig. 12 for comparison. Apparently, both Gauss–Newton and cross-adjoint methods produce good results for this data set. However, the inverted *Vs* from Gauss–Newton method are more consistent with the SPT *N*-values in both trend and magnitudes, particularly at SPT-1 and SPT-4. The cross-adjoint 3-D FWI tends to overshoot the low-velocity zones.

5 CONCLUSION

A new 3-D FWI method based on the time-domain Gauss–Newton inversion is presented for near-surface site characterization. The method is based on a solution of 3-D elastic wave equations for wave simulation, and Gauss–Newton inversion to extract subsurface wave velocities *Vs* and *Vp*. The method was tested on both synthetic and measured field data sets. The results from synthetic data set suggest that the presented waveform inversion can characterize variable high- and low-velocity subsurface layers. For the field data, both *Vs* and *Vp* of variable soil layers are characterized at metre-scales to 18-m depth with only surface-based waveform data. There is good agreement between the *Vs* and SPT *N*-values, including the identification of a buried low-velocity zone. Results from Gauss–Newton inversion are more consistent to the SPT *N*-values than those from cross-adjoint inversion.

ACKNOWLEDGEMENTS

This study was financially supported by the National Science Foundation: grant CMMI-1637557, and Florida Department of Transportation (FDOT): grant BDV31-977-82. The supports are greatly acknowledged. The authors would like to thank the FDOT State Materials Office in Gainesville, FL for providing access to the test site and conducting the SPT data.

REFERENCES

Ben-Hadj-Ali, H., Operto, S. & Virieux, J., 2008. Velocity model building by 3-D frequency-domain, full-waveform inversion of wide-aperture seismic data, *Geophysics,* **73**(5), VE101–VE117.

Butzer, S., Kurzmann, A. & Bohlen, T., 2013. "3D elastic full-waveform inversion of small-scale heterogeneities in transmission geometry", *Geophys. Prospect.,* **61,** 1238–1251.

Epanomeritakis, I., Akcelik, V., Ghattas, O. & Bielak, J., 2008. A Newton-CG method for large-scale three-dimensional elastic full waveform seismic inversion, *Inverse Problems* **24,** 26.

Fathi, A., Kallivokas, L. & Poursartip, B., 2015. Full waveform inversion in three-dimensional PML-truncated elastic media, *Comput. Methods Appl. Mech. Eng.,* **1408,** 6221

Fathi, A., Poursartip, B., Stokoe, K.H. & Kallivokas, L., 2016. Three-dimensional P-and S-wave velocity profiling of geotechnical sites using full-waveform inversion driven by field data, *Soil Dyn. Earthq. Eng.,* **87,** 63–81.

Fichtner, A., Kennett, B., Igel, H. & Bunge, H.P., 2009. Full seismic waveform tomography for upper-mantle structure in the Australasian region using adjoint methods, *Geophys J. Int.,* **179,** 1703–1725.

Ha, W., Kang, S. & Shin, C., 2015. 3D Laplace-domain waveform inversion using a low-frequency time-domain modeling algorithm, *Geophysics,* **80**(1), R1–R13.

Komatitsch, D. & Martin, R., 2007. An unsplit convolutional perfectly matched layer improved at grazing incidence for the seismic wave equation, *Geophysics,* **72**(5), SM155–SM167.

Ma, Y. & Hale, D., 2013. Wave-equation reflection traveltime inversion with dynamic warping and full-waveform inversion, *Geophysics,* **78,** R223–R233.

Métivier, L., Brossier, R., Operto, S. & Virieux, J., 2017. Full waveform inversion and the truncated newton method: SIAM Review, **59,** 153–195.

Métivier, L., Brossier, R., Virieux, J. & Operto, S., 2013. Full waveform inversion and the truncated newton method, *SIAM J. Scient. Comput.,* **35,** B401–B437.

Métivier, L., Brossier, R., Mérigot, Q., Oudet, E. & Virieux, J., 2016. An optimal transport approach for seismic tomography: Application to 3D full waveform inversion, *Inverse Problems,* **32,** 115008.

Nocedal, J. & Wright, S.J., 2006. *Numerical Optimization,* 2nd edn, Springer.

Nguyen, D.T. & Tran, K.T., 2018. "Site characterization with 3-D elastic full waveform tomography", *Geophysics,* **83**(5), R389–R400.

Pan, W., Innanen, K.A., Margrave, G.F. & Cao, D., 2015. Efficient pseudo-Gauss-Newton full waveform inversion in the *t - p* domain, *Geophysics,* **80,** R225–R14.

Plessix, R., 2009. Three-dimensional frequency-domain full-waveform inversion with an iterative solver, *Geophysics,* **74,** WCC149–WCC157.

Pratt, R.G., Shin, C. & Hicks, G.J., 1998. Gauss-Newton and full Newton methods in frequency-space seismic waveform inversion, *Geophys J. Int.,* **133,** 341–362.

Robertsson, J.O.A., 1996. A numerical free-surface condition for elastic/viscoelastic finite-difference modeling in the presence of topography, *Geophysics,* **61,** 1921–1934.

Sheen, D.H., Tuncay, K., Baag, C.E. & Ortoleva, P.J., 2006. Time domain Gauss–Newton seismic waveform inversion in elastic media, *Geophys J. Int.,* **167,** 1373–1384.

Sirgue, L., Barkved, O., Dellinger, J., Etgen, J., Albertin, U. & Kommedal, J., 2010. Full waveform inversion: the next leap forward in imaging at Valhall, *First Break,* **28,** 65–70.

Tape, C., Liu, Q., Maggi, A. & Tromp, J., 2010. Seismic tomography of the southern California crust based on spectral-element and adjoint methods, *Geophys J. Int.,* **180,** 433–62.

Tran, K.T. & Luke, B., 2017. Full waveform tomography to resolve desert alluvium, *Soil Dyn. Earthq. Eng.,* **9,** 1–8.

Tran, K.T., McVay, M., Faraone, M. & Horhota, D., 2013. Sinkhole detection using 2-D full seismic waveform tomography, *Geophysics,* **78**(5), 175–183.

Tran, K.T. & McVay, M., 2012. Site characterization using Gauss-Newton inversion of 2-D full seismic waveform in time domain, *Soil Dyn. Earthq. Eng.,* **43,** 16–24.

Vigh, D., Kapoor, J., Moldoveanu, N. & Li, H., 2011. Breakthrough acquisition and technologies for subsalt imaging, *Geophysics* **76**(5), WB41–WB51.

Virieux, J., 1986. P–SV wave propagation in heterogeneous media: velocity–stress finite-difference method, *Geophysics,* **51**(4), 889–901

Vireux, J. & Operto, S., 2009. An overview of full-waveform inversion in exploration geophysics, *Geophysics,* **74**(6), WCC1–WCC26.

Warner, M., Ratcliffe, A., Nangoo, T., Morgan, J., Umpleby, A. & Shah, N., 2013. Anisotropic 3D full-waveform inversion, *Geophysics,* **78**(2), R59–R80.